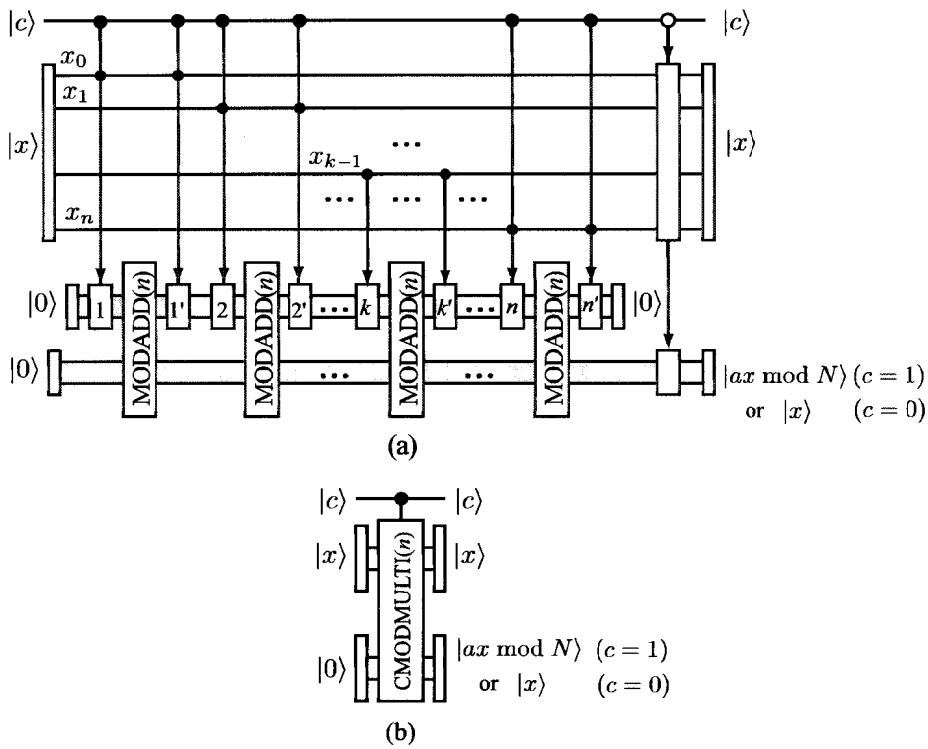

FIGURE 8.11
(a) Quantum circuit of an n-qubit controlled-modular multiplexer CMODMULTI(n). There are n layers of MODADD(n), where the kth layer adds $a2^{k-1}$ mod N to the second register when $c = 1$ and $x_{k-1} = 1$. The numbers a and N are fixed and are hardwired. The output of the second register is ax mod N. This circuit is denoted as (b), where the temporary register has no external input and output ports and is not shown explicitly.

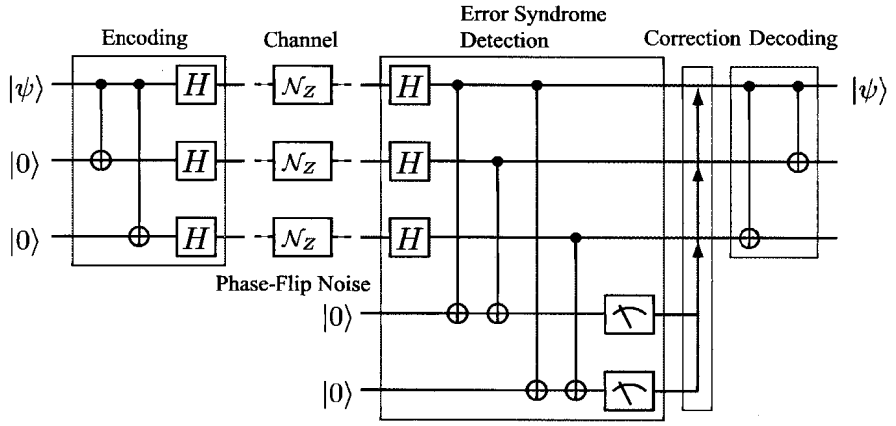

FIGURE 10.4
Three-qubit phase-flip error QECC.

$a|--+\rangle + b|++-\rangle$. We found in the above exercise that a phase-flip error acts as a bit-flip error in the basis $|\pm\rangle$; $U_{\rm H} Z U_{\rm H} = X$. Therefore, we need to put the basis back from $|\pm\rangle$ to $\{|0\rangle, |1\rangle\}$ by applying the second Walsh-Hadamard transform $U_{\rm H}^{\otimes 3}$ so that a phase-flip error is recognized as a bit-flip error and we can employ the same error syndrome detection circuit as well as the error correction circuit as those used for the bit-flip error QECC.

Collecting these results, the quantum circuit for the phase-flip QECC is constructed as shown in Fig. 10.4.

EXERCISE 10.3 Show that the circuit depicted in Fig. 10.4 is able to correct also a continuous error $U_\beta = e^{i\beta Z}$ acting on one of the qubits.

10.3 Shor's Nine-Qubit Code

Let us consider a more general noisy channel in which all possible single-qubit errors occur. Namely, the following errors are now active in the channel;

$$\begin{aligned} \text{Bit-Flip Error} \quad & X : \begin{pmatrix} a \\ b \end{pmatrix} \mapsto \begin{pmatrix} b \\ a \end{pmatrix} \\ \text{Phase-Flip Error} \quad & Z : \begin{pmatrix} a \\ b \end{pmatrix} \mapsto \begin{pmatrix} a \\ -b \end{pmatrix} \\ \text{Phase- and Bit-Flip Error} \quad & Y : \begin{pmatrix} a \\ b \end{pmatrix} \mapsto \begin{pmatrix} -b \\ a \end{pmatrix}. \end{aligned} \tag{10.13}$$

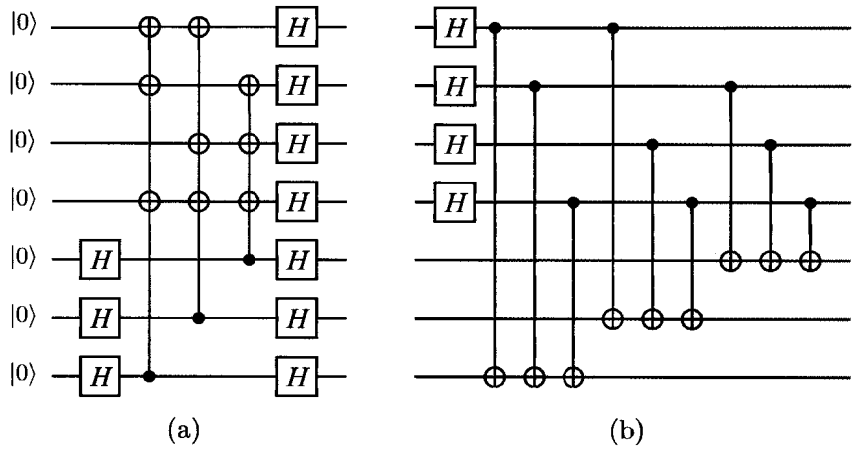

FIGURE 10.14
(a) Seven Hadamard gates applied on the logical qubit state $|x\rangle_L$. (b) A circuit equivalent with (a).

and

$$\begin{aligned}\bar{Z}|1\rangle_L &= \frac{1}{\sqrt{8}}(I+M_0)(I+M_1)(I+M_2)\bar{Z}|1\rangle^{\otimes 7} \\ &= -|1\rangle_L, \end{aligned} \tag{10.48}$$

where we noted that $[\bar{Z}, M_i] = 0$ and $(-1)^7 = -1$.

Next, we consider the Haramard gate $\tilde{H}$ acting on the encoded states as

$$\tilde{U}_{\rm H}|0\rangle_L = \frac{1}{\sqrt{2}}(|0\rangle_L + |1\rangle_L),\ \tilde{U}_{\rm H}|1\rangle_L = \frac{1}{\sqrt{2}}(|0\rangle_L - |1\rangle_L). \tag{10.49}$$

Surprisingly, this gate is also implemented by a tensor product of seven Hadamard gates,

$$\tilde{U}_{\rm H} = U_{\rm H}^{\otimes 7} = W_7, \tag{10.50}$$

where W_7 is the Walsh-Hadamard transform acting on seven qubits.

Let us consider the action of W_7 on $|0\rangle_L$ first. The circuit

$$W_7|0\rangle_L = W_7\frac{1}{\sqrt{8}}(I+M_0)(I+M_1)(I+M_2)|0\rangle^{\otimes 7}$$

given in Fig. 10.14 (a) is put in the form given in (b) by making use of the trick introduced in Fig. 10.9 and $U_{\rm H}^2 = I$. The resulting circuit is written as

$$\begin{aligned} W_7|0\rangle_L &= [{\rm C}_0(X_6X_5)][{\rm C}_1(X_6X_4)][{\rm C}_2(X_5X_4)] \\ &\quad \times[{\rm C}_3(X_6X_5X_4)]U_{\rm H0}U_{\rm H1}U_{\rm H2}U_{\rm H3}|0\rangle^{\otimes 7} \\ &= [{\rm C}_0(X_6X_5)U_{\rm H0}][{\rm C}_1(X_6X_4)U_{\rm H1}][{\rm C}_2(X_5X_4)U_{\rm H2}] \\ &\quad \times[{\rm C}_3(X_6X_5X_4)U_{\rm H3}]|0\rangle^{\otimes 7}, \end{aligned} \tag{10.51}$$

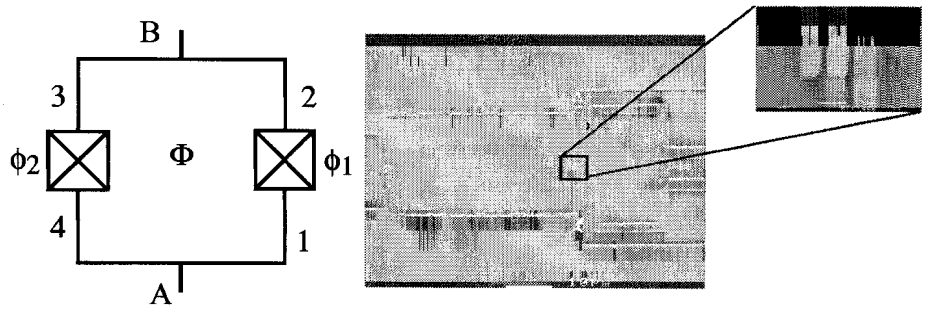

FIGURE 15.4
(a) Schematic diagram of a SQUID with two Josephson junctions. (b) Actual nanoscale SQUID. The enlarged structure is the Josephson junction in Fig. 15.1. The white line in the bottom is 10 μm long. Courtesy of Jukka Pekola, Helsinki University of Technology, Finland.

where we assumed that the two Josephson junctions are identical and each junction has the Josephson energy $E_J/2$. By introducing the parameters

$$\delta = \phi_1 - \phi_2 = 2\pi\frac{\Phi}{\Phi_0}, \quad \phi = \frac{\phi_1 + \phi_2}{2}, \tag{15.22}$$

the Josephson energy is rewritten as

$$E = -E_J \cos\frac{\delta}{2}\cos\phi. \tag{15.23}$$

The factor $\cos(\delta/2)$ in the RHS is due to the interference between Cooper pairs through two paths and hence is regarded as a manifestation of the Bohm-Aharonov effect. The current through junction 1, in the direction from A to B, is

$$I_1 = \frac{I_c}{2}\sin\phi_1,$$

while that through the junction 2, from A to B, is

$$I_2 = \frac{I_c}{2}\sin\phi_2,$$

where $I_c \equiv 2eE_J/\hbar$. Therefore the current through the SQUID from A to B in Fig. 15.4 (a) is

$$J = I_1 + I_2 = \frac{2e}{\hbar}\frac{\partial E}{\partial\phi}. \tag{15.24}$$

Note that a current flows along the SQUID loop even when $I_1 = -I_2$, for

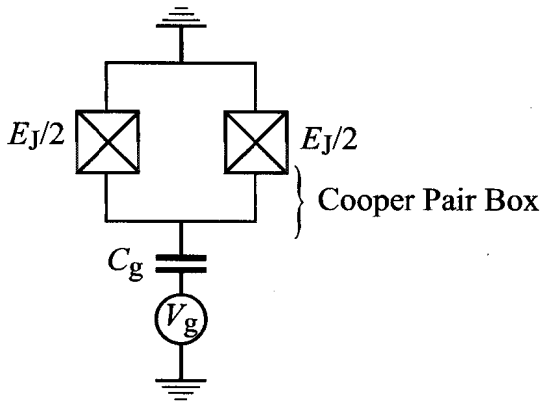

FIGURE 15.8
Charge qubit with a tunable Josephson energy.

15.3.2 Split Cooper Pair Box

It has been shown in §15.2.2 that a superconducting loop with two idential Josephson junctions with identical Josephson energy $E_J/2$ has the total Josephson energy

$$-\frac{E_J}{2}(\cos\phi_1 + \cos\phi_2) = -E_J \cos\frac{\phi_1+\phi_2}{2}\cos\frac{\phi_1-\phi_2}{2}, \tag{15.46}$$

where ϕ_1 and ϕ_2 are the phase differences across the junctions 1 and 2, respectively. Let L be the self-inductance of the loop and I be the current circulating the loop. Then the difference $\phi_1 - \phi_2$ is related to the magnetic flux $\Phi = \Phi_{\text{ext}} + LI$ threading the loop as

$$\frac{\phi_1-\phi_2}{2} = \pi\frac{\Phi}{\Phi_0} \simeq \pi\frac{\Phi_{\text{ext}}}{\Phi_0}, \tag{15.47}$$

where we assumed that the self-inductance L is very small for a charge qubit under consideration. Now the Josephson energy is expressed as

$$-E_J \cos\left(\pi\frac{\Phi_{\text{ext}}}{\Phi_0}\right)\cos\phi, \tag{15.48}$$

where $\phi = (\phi_1 - \phi_2)/2$. It has been shown that the effective Josephson energy is given by

$$E_J(\Phi) = E_J \cos\left(\pi\frac{\Phi_{\text{ext}}}{\Phi_0}\right). \tag{15.49}$$

Figure 15.8 shows a schematic picture of a charge qubit with a tunable Josephson energy, called a **split Cooper pair box.** The total Hamiltonian

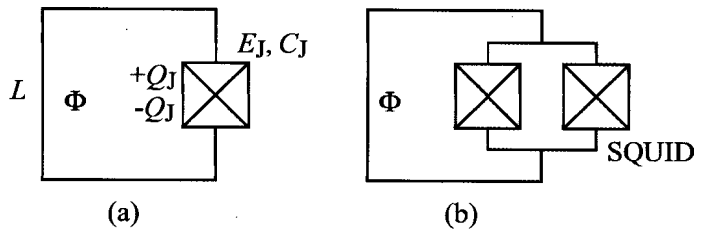

FIGURE 15.9
Simplest flux qubits. (a) An rf-SQUID and (b) a flux qubit with a tunable Josephson energy E_J.

is again given by

$$H = -\frac{1}{2}B_z(N_g)\sigma_z - \frac{1}{2}B_x(\Phi_{\text{ext}})\sigma_x, \tag{15.50}$$

where both coefficients

$$B_z(N_g) = \frac{E_C}{2}(1-2N_g),\ B_x(\Phi_{\text{ext}}) = E_J\cos\left(\pi\frac{\Phi_{\text{ext}}}{\Phi_0}\right) \tag{15.51}$$

are controllable.

The eigenvalues and the corresponding eigenvectors of the Hamiltonian (15.50) are given by Eqs. (15.43) and (15.44) with B_x in Eq. (15.45) replaced by $B_x(\Phi_{\text{ext}})$. Observe that $|0\rangle \to |N=0\rangle$ and $|1\rangle \to |N=1\rangle$ as $\Phi_{\text{ext}} \to \Phi_0/2$ with $B_z(N_g) \neq 0$, while $|0\rangle \to (|N=0\rangle + |N=1\rangle)/\sqrt{2}$ and $|1\rangle \to (-|N=0\rangle + |N=1\rangle)/\sqrt{2}$ as $N_g \to 1/2$ with $B_x(\Phi_{\text{ext}}) \neq 0$.

15.4 Flux Qubit

In contrast with a charge qubit, the flux threading a SQUID is the relevant degree of freedom in a flux qubit. Here we need to employ a circuit with

$$E_J \gg E_C. \tag{15.52}$$

15.4.1 Simplest Flux Qubit

The simplest flux qubit, the **rf-SQUID**, is shown in Fig. 15.9. This is nothing but a SQUID with no input/output current. It is made of a superconducting loop with a Josephson junction where the loop supports a persistent current I and a flux Φ threading the loop. The flux is related to the external magnetic

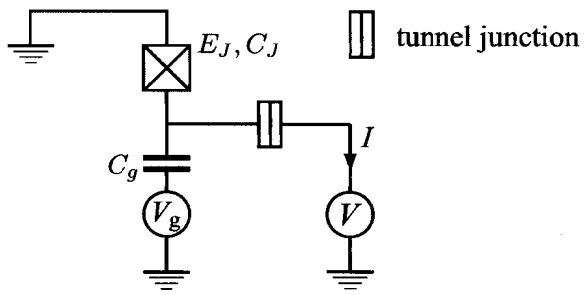

FIGURE 15.15
Direct observation of the charge qubit state by measurement of a current through a tunnel junction.

state is approximately the same as the state $|N = 0\rangle$, and the system is in this state with a large probability. Next a gate pulse with the pulse width Δt is applied so that N_g is now equal to 0.5 ($B_z = 0$) during this period. Finally the gate voltage is put back to its initial value. Suppose the risetime and falltime of pulses are much shorter than $\hbar/E_J$. Let us analyze the state evolution associated with this pulse, following Fig. 15.16. (i) The system is in the state $|N = 0\rangle = (|0\rangle - |1\rangle)/\sqrt{2}$ immediately after the pulse is turned on, and the Bloch vector starts to rotate around the x-axis for the period Δt due to the E_J-term (B_x), which implies that the sytem oscillates between $|N = 0\rangle$ and $|N = 1\rangle$ (**Rabi oscillation**). (ii) When the pulse is turned off, the state is a superposition of $|N = 0\rangle$ and $|N = 1\rangle$ whose coefficients are determined by Δt. The state $|N = 1\rangle$ has considerably higher energy than $|N = 0\rangle$ without the pulse, viz $N_g = 0.25$. Suppose the tunneling bias voltage V is adjusted so that the quasiparticle energy outside the Josephson junction sits between those of $|N = 0\rangle$ and $|N = 1\rangle$ states. Then the state $|N = 1\rangle$ decays into two quasiparticles and the electric current I, associated with these quasiparticles, is detected, while the $|N = 0\rangle$ state, in contrast, is stable against this decay. This is how the qubit states $|N = 0\rangle$ and $|N = 1\rangle$ are discriminated by measuring the tunneling current. Another advantage of this method is that if one waits for some duration of time required for the $|N = 1\rangle$ state to dacay into two quasiparticles after the pulse is turned off, the qubit is definitely in the initial state $|N = 0\rangle$. Therefore, by repeating the above process many times with a fixed Δt, the probability of the qubit in the state $|N = 1\rangle$ is found by tunneling current measurements.

Figure 15.17 shows the Rabi oscillation observed in this way. The phase decoherence time T_2 has been also measured by using the same readout method [12].

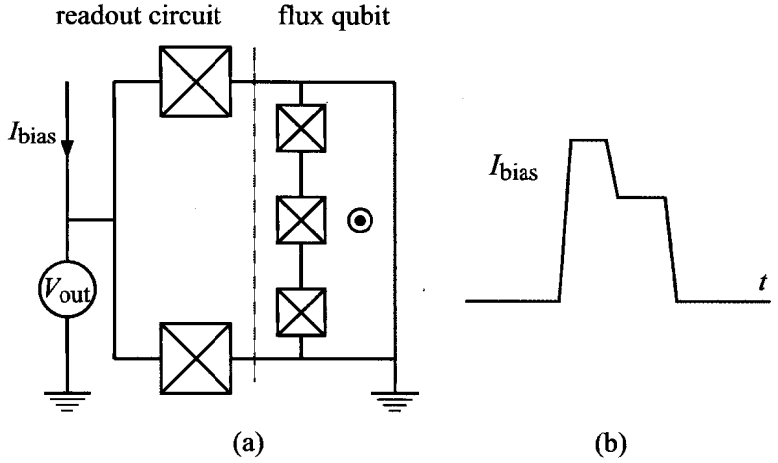

FIGURE 15.19
(a) A flux qubit with readout SQUIDs. (b) Bias current I_{bias} for readout. Transition to normal state manifests itself as finite V_{out}.

a small probability with which the voltage $V(t) \neq 0$ is observed even in the CPB state $|0\rangle$. Let p_0 and p_1 be the probabilities with which the junction undergoes a transition to the normal state when the CPB is in the states $|0\rangle$ and $|1\rangle$, respectively. A theoretical estimate shows that $p_1 - p_0 = 0.95$ while the observed value is ~ 0.6. However this discrepancy does not matter in the estimation ~ 1.8 μs of T_1. The phase decoherence time T_2 has also been measured by making use of the Ramsey fringe experiment [8] and spin-echo-type technique. The value they obtained is $T_2 \sim 0.50$ μs, corresponding to approximately 8,000 free precessions.

15.7.3 Switching Current Readout of Flux Qubits

Readout of a flux qubit is conducted in a similar manner as that of a quantronium [16, 17]. Figure 15.19 (a) shows a typical circuit for flux qubit readout, in which a readout dc SQUID with two junctions is connected to a three-junction flux qubit [17]. The circuit may support a bias current I_{bias}, and a voltmeter measures the voltage V_{out} while the bias current is applied.

Readout is carried out with the bias current I_{bias}. The current I_{bias} comprises a short pulse and a succedent trailing plateau as shown in Fig. 15.19 (b). The flux qubit is driven to normal state by a short pulse depending on its qubit state, and the trailing plateau is applied to prevent the qubit from reentering the superconducting state.

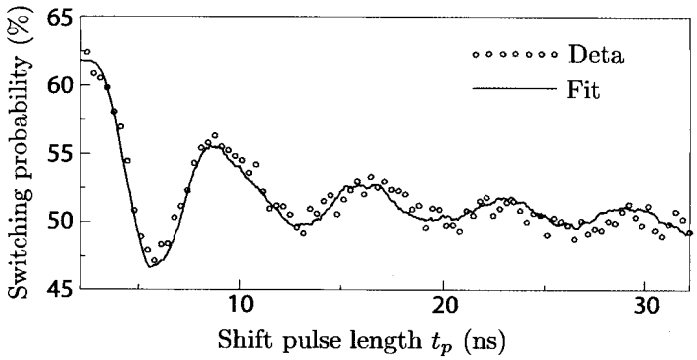

FIGURE 15.26
Switching probability, which reveals vacuum Rabi oscillation, as a function of the pulse length t_p [ns]. Reprinted figure with permission from J. Johansson *et al.*, Physical Review Letters **96**, 127006 (2006), Copyright (2006) by the American Physical Society.

The Hamiltonian at the degeneracy point 3 is H_i, and it follows from Eq. (15.134) that the relevant matrix element is

$$(\langle 0|\langle n=1|)\ H_i\ (|1\rangle|n=0\rangle) = i2\hbar\lambda \sin\frac{\alpha}{2}\cos\frac{\alpha}{2}. \tag{15.148}$$

The eigenstates of the Hamiltonian are $(|1\rangle|n=0\rangle \pm i|0\rangle|n=1\rangle)/\sqrt{2}$, and the corresponding eigen energies are $\pm\hbar\lambda\sin\alpha$. Therefore the Rabi oscillation frequency is given by $\Omega_R = 2\lambda\sin\alpha$. Finally the shift pulse is turned off so that Φ_{ext} assumes its initial value at $t=0$. The resulting states are $|0\rangle|n=1\rangle$ and $|1\rangle|n=0\rangle$ denoted as 4 and 2, respectively, in Fig. 15.25. Then a readout process is applied to the state. Figure 15.26 shows the measurement result.

The CNOT gate in trapped ions has been implemented by introducing effective coupling between distant ions through mediating phonon mode. It has been pointed out recently that a similar mechanism might work for flux qubits if the phonon mode in trapped ions is replaced by the plasmon mode in the LC resonator. The coupling between the qubit and the resonator is made possible through the mutual inductance.

It is shown in a recent proposal by the NTT group [23] that a flux qubit-flux qubit coupling may be introduced by coupling them selectively to an LC resonator whose resonace frequency is controllable by adjusting the bias current through the Josephson junction in the LC circuit. An explicit protocol to entangle arbitrary two flux qubits among many qubits is proposed, in which a resonating circuit surrounding these qubits is made use of. The theoretical proposal of this scenerio has been already reported, and experiments demonstrating this qubit-qubit coupling are planned [23].

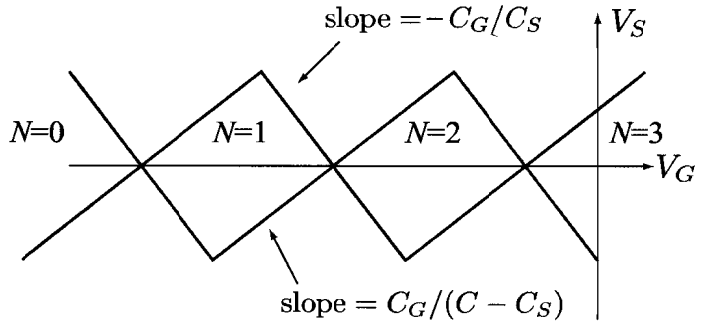

FIGURE 16.6
Coulomb blockade diamond. The parallelogram made of lines with a slope $-C_G/C_D$ and lines with a slope $C_G/(C - C_S)$ is a Coulomb blockade region in the $V_G - V_S$ plane. The number of electrons is fixed in the Coulomb blockade region. The diagram shows the region where $N = 0, 1, 2$ and 3. The region corresponding to $N = 0$ is exceptional in that the diamond does not close, and hence it is discriminated from the other diamonds.

each parallelogram decreases as V_G is lowered; see Fig. 16.6. The state with $N = 0$ appears in the left end of V_G axis, which is easily identifiable since the corresponding "parallelogram" does not close. The failure of the closure is attributed to the fact that the conditions (a) and (b) are not necessary in this region. States with small N, such as $N = 1$ or 2, are prepared by making use of this fact.

It is found from the above observation that the Coulomb blockade phenomena, with which a given electron number state stabilizes the QD, plays a very important role when a QD is employed as a qubit.

16.3 Electron Charge Qubit

Two types of qubits that make use of electronic states in quantum dots are proposed to date. One uses two neighboring quantum QDs, which we call the **double quantum dots** or DQD for short in the following, and the two different states $|0\rangle$ and $|1\rangle$ of a qubit correspond to which of the two QDs is occupied. This qubit is called a **charge qubit**. The other qubit, called a **spin qubit**, makes use of two spin states, spin up and spin down, of an electron trapped in a single quantum dot.

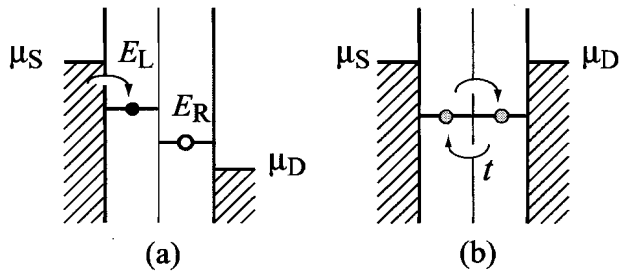

FIGURE 16.8
(a) Energy diagram of DQD when $\mu_D < E_R < E_L < \mu_S$. (b) The same for the case $E_L = E_R < \mu_S = \mu_D$, where t is the overlap integral.

be described by Eqs. (16.8) and (16.9), temperature must be low enough and moreover $|\varepsilon|$ and Δ must be small enough compared to the energy level separation due to Coulomb blockade.

16.3.2 Rabi Oscillation

Rabi oscillation in an electron charge qubit has been first observed by the NTT group [4]. Initialization and measurements were made in the state shown in Fig. 16.8 (a). This state satisfies the conditions $\mu_S > E_L > E_R > \mu_D$ and $|\varepsilon| \gg \Delta$. The gate electrode voltages are controlled first to make the system in the state shown in Fig. 16.8 (a). An electron is supplied from the source S, and the relevant energy level of the left QD is occupied so that the state $(N_L + 1, N_R)$ is realized. This electron does not hop to the right QD due to the assumption $|\varepsilon| \gg \Delta$. Next the DQD is steered to a state with $\mu_S = \mu_D > E_L = E_R$ so that $\varepsilon = 0$ as shown in Fig.16.8 (b). Then the DQD is detached from S and D and allowed to execute Rabi oscillation for the duration t_P, after which the system is further driven back to the state in Fig. 16.8 (a). The coupling between the QDs is turned off in this state and only the electron residing in the right dot flows into D and the system is put back to the initial state. The signal obtained in a single measurement is not strong enough to be observed. Hayashi *et al.* measured the current I flowing out from D by repeating the above cycle many times [4]. Figure 16.9 shows experimentally observed Rabi oscillation.

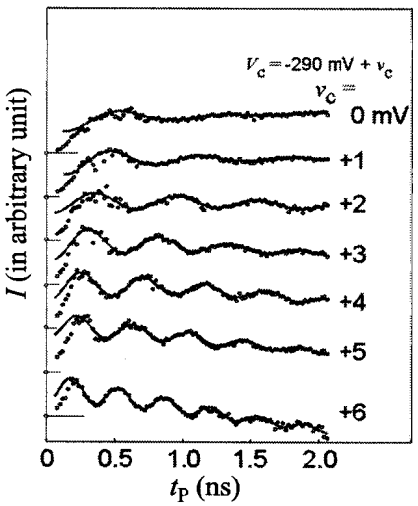

FIGURE 16.9
Coherent charge oscillation. The barrier height between the left and the right dots is controlled by changing the paramter V_C, which changes the overlap intergral t and hence Δ, leading the change in the Rabi oscillation frequency. Courtesy of NTT Basic Research Laboratory.

16.4 Electron Spin Qubit

16.4.1 Electron Spin Qubit

Let us consider an electron confined in a QD. We define the logical state $|0\rangle$ as the spin-$\uparrow$ state and the logical $|1\rangle$ as the spin-$\downarrow$ state. Technology making use of electron spins thus defined is called **spintronics** in the literature. The electron number N for a spintronics is 1 in an ideal situation. A QD with $N = 1$ is easily realized not only in a QD but also in a DQD as mentioned in the previous section. Let us consider a DQD and let $\boldsymbol{S}_L$ ($\boldsymbol{S}_R$) be the spin operator of the left (right) QD. Two-qubit coupling is given by

$$H_{int} = J \sum_{k=x,y,z} S_k \otimes S_k, \tag{16.10}$$

where the exchange energy J is controllable by changing the overlap intergral between the electron wave functions. This is done by changing the barrier height between the dots by controlling the voltage applied to the electrodes separating the dots.

Although coherent motion of a large number of spins is well established in

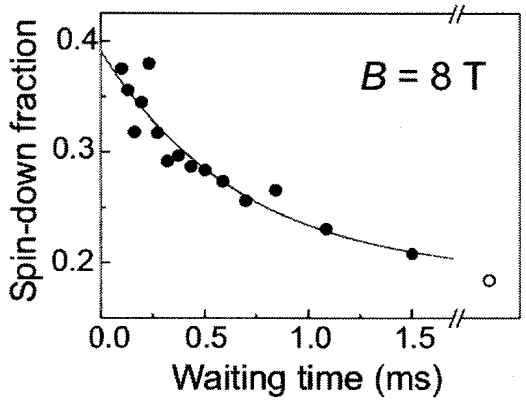

FIGURE 16.12
Measurement of the spin-relaxation time T_1. Relaxation from the spin-down state to the spin-up state takes place in waiting time t_{wait}. Electron injection to the dot takes place slightly after V_P is set to 2). This delay is so short, however, that it may be negligible in practice [6]. Courtesy of Jeroen Elzerman, ETH, Switzerland.

the spin is observed in the $\downarrow$-state as the pulse width in Step 2 is changed. The relaxation time T_1 measured in this way is $\sim 0.85 \pm 0.11$ ms at a magnetic field of 8 T.

16.4.3 Coherence Time

Suppose there is a single electron in a quantum dot. It is reported that the longitudinal relaxation time T_1 of the electron is as long as $\sim$ 10 ms [5]. The coherence time T_2^*, which is defined as the phase relaxation time experimentally observed, is on the order of ~ 10 ns. An electron in a quantum dot is under fluctuating magnetic field produced by Ga and As nuclear spins, which couples with the electron through the hyperfine interaction. Each dot has $\sim 10^6$ nuclear spins of Ga and As, which thermally fluctuate. The effective magnetic field on the electron is known to fluctuate with the time scale on the order of ~ 10 μs.

Let us turn to the measurement of the dephasing time T_2. Single-shot signal strength is, however, not strong enough to directly read out T_2. Signals are accumulated during the interval longer than the typical fluctuation time of the nuclei. Therefore the observed phase decoherence time is obtained by averaging a snap-shot T_2 over ensemble under fluctuating magnetic field. The decoherence time thus obtained is denoted as T_2^*. It is found from the observed value $T_2^* = 10$ ns that the amplitude of the nuclear magnetic field

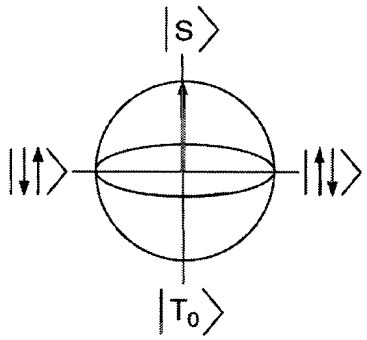

FIGURE 16.15
Bloch sphere, which represents a DQD state in $(1,1)$. The north pole and the south pole of the Bloch sphere corresponds to the singlet state $|S\rangle$ and the triplet state $|T_0\rangle$, respectively, while $|\uparrow\downarrow\rangle$ and $|\downarrow\uparrow\rangle$ are in the xy-plane. The arrow shows the initial state $|S\rangle$. Reprinted from Physica E, **35**, J. R. Petta *et al.*, "Preparing, manipulating, and measuring quantum states on a chip", 251–256, Copyright (2006), with permission from Elsevier.

is called the **spin blockade** and is employed as a readout method of qubit states in this exeperiment. In the state $(1,1)$ on the other hand, the energies of the three states of a triplet electron pair and that of the singlet pair are almost degenerate if the exchange energy J is negligible. If a magnetic field is applied in this state, the $|\uparrow\uparrow\rangle$ and $|\downarrow\downarrow\rangle$ states have different energies, while that of the residual states, a singlet state $|S\rangle = (|\uparrow\downarrow\rangle - |\downarrow\uparrow\rangle)/\sqrt{2}$ and a triplet state $|T_0\rangle = (|\uparrow\downarrow\rangle + |\downarrow\uparrow\rangle)/\sqrt{2}$, remain degenerate. We choose $|S\rangle$ and $|T_0\rangle$ as the qubit states $|0\rangle$ and $|1\rangle$, respectively. Any qubit state is expressed as a point on a Bloch sphere as shown in Fig. 16.15. In fact, the degeneracy between $|S\rangle$ and $|T_0\rangle$ is lifted if the exchange interaction J between the dots is taken into account. As a result, the energy of the singlet state S is lower than that of the triplet state T_0 by J. The parameter J is controllable by changing ε (≤ 0). It takes maximum value $J(0)$ when $\varepsilon = 0$ and $J(\varepsilon) \to 0$ in the limit $|\varepsilon| \gg J(0)$. Let $B^L_{\rm nuc}$ ($B^R_{\rm nuc}$) be the component of the hyperfine field in the left (right) dot. Then the Hamiltonian of this qubit is

$$H = \begin{pmatrix} 0 & g^*\mu_B \Delta B_{\rm nuc} \\ g^*\mu_B \Delta B_{\rm nuc} & J(\varepsilon) \end{pmatrix}, \tag{16.11}$$

where $g^* \simeq -0.44$ is the electron g factor in GaAs, μ_B is the Bohr magneton, $\Delta B_{\rm nuc} \equiv B^L_{\rm nuc} - B^R_{\rm nuc}$ and $J(0) \gg |\Delta B_{\rm nuc}|$.

The intrinsic phase coherence time T_2 of this qubit has been measured by elimimating the effect of the nuclear magnetic field fluctuation. The parameter ε has been scanned in the spin-echo experiment as shown in Fig. 16.16.

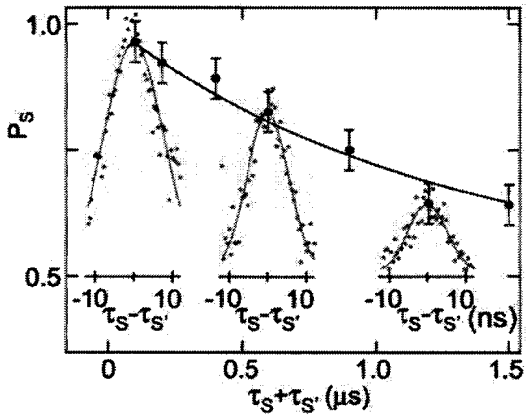

FIGURE 16.17
Spin echo recovery probability P_S plotted against $\tau_S - \tau_{S'}$ for given $\tau_S + \tau_{S'}$. Observe that the probability takes the maximum value at $\tau_S - \tau_{S'} = 0$. The coherence time T_2 is obtained by plotting the maximum value as a function of $\tau_S + \tau_{S'}$. From J. R. Petta *et al.*, SCIENCE, **309**: 2180-2184 (30 September 2005) and J. R. Petta *et al.*, Physica E, **35**, 251-256 (December 2006). Reprinted with permissions from AAAS and Elsevier.

16.5 DiVincenzo Criteria

DiVincenzo criteria for a quantum dot quantum computer are evaluated separately for charge qubits and spin qubits.

16.5.1 Charge Qubits

Let us evaluate the DiVincenzo criteria for charge qubits.

1. A scalable physical system with well-characterized qubits:

   A qubit is made of a double quantum dot fabricated in a GaAs/Al/GaAs heterostructure. It is potentially scalable using currently available semiconductor lithography technology. A two-qubit system has been fabricated, and coupling between two qubits has been demonstrated so far [10]. The two basis states of the qubit correspond to states in which an electron sits in the right (left) quantum dot.

2. The ability to initialize the state of the qubits to a simple fiducial state, such as $|00\ldots0\rangle$:

   The qubit can be initialized by electron injection [4]; see Fig. 16.8.